Development and characterization of Fe-30Cu-10Si-6W-10Mo superalloy with enhanced γ′ phase stability and oxidation resistance using CALPHAD method

Suresh Kumar K[1], Mohanraj K[2*], Muhammadu Sathik Raja[3], Arul M[4], Beporam Iftekhar Hussain[5], Nanthakumar S[6] and Devarajan R[7]

[1]Department of MBA, Panimalar Engineering College, Tamil Nadu, India
[2]Department of Automobile Engineering, Rajalakshmi Engineering College, Tamil Nadu, India.
[3]Department of Medical Electronics, Sengunthar Engineering College, Tamil Nadu, India
[4]Department of Mechanical Engineering, ARM College of Engineering and Technology, Tamil Nadu, India
[5]Department of Mechanical Engineering, Bapatla Engineering College, Andhra Pradesh, India
[6]Department of Mechanical Engineering, PSG Institute of Technology and Applied Research, Tamil Nadu, India
[7]Department of Electrical and Electronics Engineering, Vinayaka Mission's Kirupananda Variyar Engineering College, Vinayaka Mission's Research Foundation Deemed to be University, Tamil Nadu, India

*E-mail: mohanraj.k@rajalakshmi.edu.in

Abstract. The objective of the study was to develop an alloy with a significant proportion of the γ′ phase and solvus, together with an optimal thermal processing range, by employing the CALPHAD (Calculation of Phase Diagrams) approach. The alloy composition employed consisted of iron (Fe), copper (Cu), silicon (Si), tungsten (W), and molybdenum (Mo) in the proportions of 30 %, 10 %, 10 %, 6 %, and 10 % respectively. The actual results validated the calculations and showed that Mo is a constituent that forms the γ phase in Fe-Cu-Si-W-based alloys. Molybdenum (Mo) is added to the alloy to mitigate the discrepancy in lattice structure, impede the formation of bigger particles, and lower the overall density of the alloy. The inclusion of a precise amount of Mo led to the formation of a superalloy that demonstrates a combination of superior mechanical performance at the γ′ solvus and a reduced density. Furthermore, the incorporation of Mo can greatly improve the ability of the Fe-Cu-Si-W high-temperature alloy to resist oxidation. At a temperature of 1000°C, the Fe-30Cu-10Si-6W-10Mo alloy showed minimal weight gain from oxidation, demonstrating its outstanding resistance to oxidation. The primary cause of this phenomenon is the formation of continuous layers of $(Fe, Cu)(Si, Mo)_2O_4$ spinel oxide after prolonged oxidation.

Keywords: Superalloy, Characterization, Phase stability, Oxidation Resistance, CALPHAD method.

1. Introduction

Due of the lack of precipitation strengthening, traditional Fe-based superalloys displayed subpar high-temperature characteristics. New opportunities for the creation of new Fe -based superalloys have been opened up by the discovery of γ'- Fe (Si, W (Tungsten)) in the Fe - Si - Tungsten system. Superalloys based on cobalt and tungsten have a lot of potential, but their high density has limited their use in real-world applications. Which is why W-free Fe-based superalloys have been getting a lot of buzz lately. A number of Fe -based superalloys have been developed in response to this problem, using different alloy systems such as Fe - Si -Molybdenum- W, Fe - Si - Molybdenum -Niobium, Fe - W -Vanadium, Fe - Niobium - Vanadium, Fe -Titanium- Molybdenum, and Fe - Titanium – Mo [1, 2]. Nevertheless, comparisons with Fe -Si-W-based alloys reveal that these alloys have lower solvus temperatures and less stable γ' phases. Authors analysed the alloying elements effect on the metastable L12-Fe3Si phase using density functional theory (DFT) methods [3]. Their study's results indicated that elements including Tungsten, W, Vanadium, Titanium, Niobium, rhenium, Molybdenum, Platinum, and Iridium could act as stabilizers for the metastable γ'-Fe3Si phase. In Fe - Si -X ternary system, our findings lend credence to the possibility of L12-ordered γ'- Carbon trioxide (Si, X) phase. The authors developed a new system of high-temperature alloys consisting of W-free Fe - Si – W [4]. Authors' research shown that the alloy was enhanced by Ni addition, leading to a larger γ/γ' two-phase region, improved γ' solvus, and more stable γ/γ' dual-phase microstructure. Moreover, the research found that W significantly raises γ' solvus temperature and phase percentage. In addition, the paper delves further into the effects of Mo. The inclusion of Mo effects the dense and alloy misfit, while reducing the coarsening rate of γ'. The γ/γ' dual-phase microstructure is stable and well-defined in the alloy [5, 6]. The goal of the study by authors [7] was to optimize the composition of Fe -Al-Ta-based alloys using machine learning and experimental methodologies in order to improve their mechanical behaviours. Based on the findings, Co-30Ni-10Al-6Ta alloy showed remarkable compressive yield strength (CYS) and microstructure stability between 800 and 1000ºC. Because of its wide heat treatment window and greater γ' solvus, the study also found that this alloy system has the potential for further optimization. Nevertheless, additional alloying to correct the alloy density is required due to the high Ta level of the alloy. Additionally, the alloy's performance in terms of oxidation resistance was not covered in the paper. Hence, high-temperature alloys based on Co-Ni-Al-Ta still have opportunity to be improved in terms of density and oxidation resistance. Incorporating Cr into a γ/γ' with moderate mechanical behaviours and outstanding oxidation resistance is our goal in this research. Cr is known to increase superalloy oxidation resistance and decrease the coarsening rate of the γ/γ' phase. On the other hand, mechanical characteristics might be diminished by a maximum Cr contented [8]. Recent research has shown that using the CALPHAD technique for thermodynamic simulations can accelerate the development of superalloy compositions and result in improved properties [9, 10]. Hence, authors utilized the thermodynamic phase diagram prediction for percentage and γ' solvus to create multiple Fe -30 Cu -10 Si -6 W -x Mo superalloys. In addition, the study extensively investigates how Cr affects the γ' solvus, γ/γ' microstructure, oxidation resistance qualities, γ/γ' lattice misfit, and alloy density.

2. Procedures for calculations and experiments

2.1 Specimen preparation
The specimen was made with highly pure (99.9 wt.%) Fe, Cu, Si, W, and Mo. The alloy compositions are presented in the study using at percentage notation. Anhydrous ethanol was used for ultrasonic cleaning of the raw materials. Authors melted the metal at least eight times in an arc-melting furnace to make sure it was all the same. The specimens were vacuum-sealed in a quartz tube prior to heat treatment.

A small quantity of argon gas was introduced to create a protective atmosphere. In order to achieve the required microstructure at that temperature, they were subsequently satisfied in cold water. The alloy specimens were aged at 800°C for 24 hours to 200 hours after being treated in a solid solution for 12 hours at 1250°C, to achieve a refined γ/γ′ morphology. To ascertain the rate of oxidation, the large specimens were ground into uniformly sized pieces and tested in a tube furnace with an air environment. The furnace was heated to the right temperature. The specimens were meticulously placed in alumina crucibles during the oxidation tests to enable the size of the overall weightage improvement, which includes slightly oxide rate that detached. Samples were oxidized for 50, 100, 200, and 300 hours, respectively. The precise measurement of each specimen's weight growth, up to 10^{-4} g, was achieved. After taking each specimen out of the furnace, we weighed it with its crucible to acquire the mass change. We then subtracted the starting weight of the crucibles to get the final mass change.

2.2 X-ray diffraction
After oxidation at 1000°C, the lattice variables of oxide products in the alloy powders specimen and γ/γ' phase were measured using a Bruker D8 XRD apparatus that is equipped with Cu-Kα radiation. For fitting the sub-peaks extracted from (111) peak, the Pseudo-Voigt functions were used. In earlier research, this fitting method was used to examine the lattice characteristics of different alloys based on cobalt.

2.3 Mechanical properties that are compressive and thermal
A NETZSCH 404 F3 differential scanning calorimetry (DSC) was used to ascertain the phase transition temperatures of the alloys in their as-aged state. During the DSC measurements, a heating rate of 10°C/min was used. Circular specimens were manufactured for mechanical behaviour tests; their dimensions were 6 mm in height and 4 mm in diameter. Both room temperature and elevated temperatures between 600 and 900°C were used for the compression tests. During the compression tests, a continuous strain rate of 10^{-3}/s was delivered utilizing a WDW-100E test machine.

2.4 First-principal computations with CALPHAD
In this study, the phase fraction was forecasted using computed phase diagrams, and the correct composition inside the γ′/γ phase area was identified. Drawing on prior experimental and thermodynamic computations, our group established a database of Fe-based superalloy thermodynamics [11, 12]. In this case, authors used Pandat and our thermodynamic dataset to compute the phase fraction and phase diagram for the Fe - Cu - Si - W - Mo system alloy. In order to optimize geometric parameters and evaluate energy, the VASP code incorporates simulations of ab initio molecular dynamics (AIMD) [13]. To understand the interaction between the core and valence electrons, one uses the projected augmented wave technique [14]. In plane wave expansion, the kinetic energy cutoff is 520 eV, and a k-grid centered on gamma with a resolution of 0.04 (in $2\pi/\text{Å}$ units) samples the reciprocal space [15]. The energy disparity required to resolve the wave function of electronics must be contained within 1×10^{4} eV range as per the convergence criterion, and it makes use of Methfessel-Paxton 2nd-order spreading technique with a breadth of 0.07 eV. Until the force drops below 0.02 eV/Å, all atomic structures are fine-tuned. Furthermore, a second-order van der Waals density functional theory -D3 technique is used, which is based on Becke-Johnson damping [16, 17]. A standard ensemble (NVT) is used to execute all ab initio molecular dynamics simulations, with the temperature regulated by a Nose thermostat. A 1 fs time step (1 fs = 10-15 s) is used in the velocity Verlet algorithm to solve the motion equations.

3. Results and discussions

3.1 Compositional design for Fe -30 Cu -10 Si -6 W -x Mo alloys

Fig. 1(a) shows the pseudo-phase diagram of Fe -30 Cu -10 Si -6 W -x Mo, which was computed using the database our research group developed to establish a γ'/γ stable phase in superalloys at increased maximum temperatures. A significant γ'/γ' dual phase region is shown in Fe - Cu - Si - W - Mo alloy system in the diagram. The γ solvus stabilizes and gradually reductions with the addition of Mo, while the γ' solvus initially rises somewhat and then falls. In Fig. 1 (b)-(c), the computed phase fraction of Fe -30 Cu -10 Si -6 W -x Mo (x: 0, 5, 10) is shown. It is worth mentioning that the γ' phase fraction increases noticeably when the alloy contains more Mo. Fe -30 Cu -10 Si -6 W -5 Mo (6W5 Mo), Fe -30 Cu -10 Si -6 W -10 Mo (6W10 Mo), and Fe -30 Cu -10 Si -6 W -6Ta allotments have predicted phase fractions of 41.9%, 43%, and 48.7%, respectively. A significant decrease in the γ' solvus is clearly shown by the phase diagram as a result of an alloy with a high Mo concentration. Furthermore, the alloy's mechanical qualities could be negatively affected by a high concentration of Mo, which would restrict its usefulness in high-temperature applications. So, instead of going into detail about alloys with high Mo concentrations, this study will concentrate on Fe -30 Cu -10 Si -6 W -x Mo (x: 5, 10) alloys, with the goal of creating alloys with improved mechanical properties, oxidation resistance, and γ' solvus.
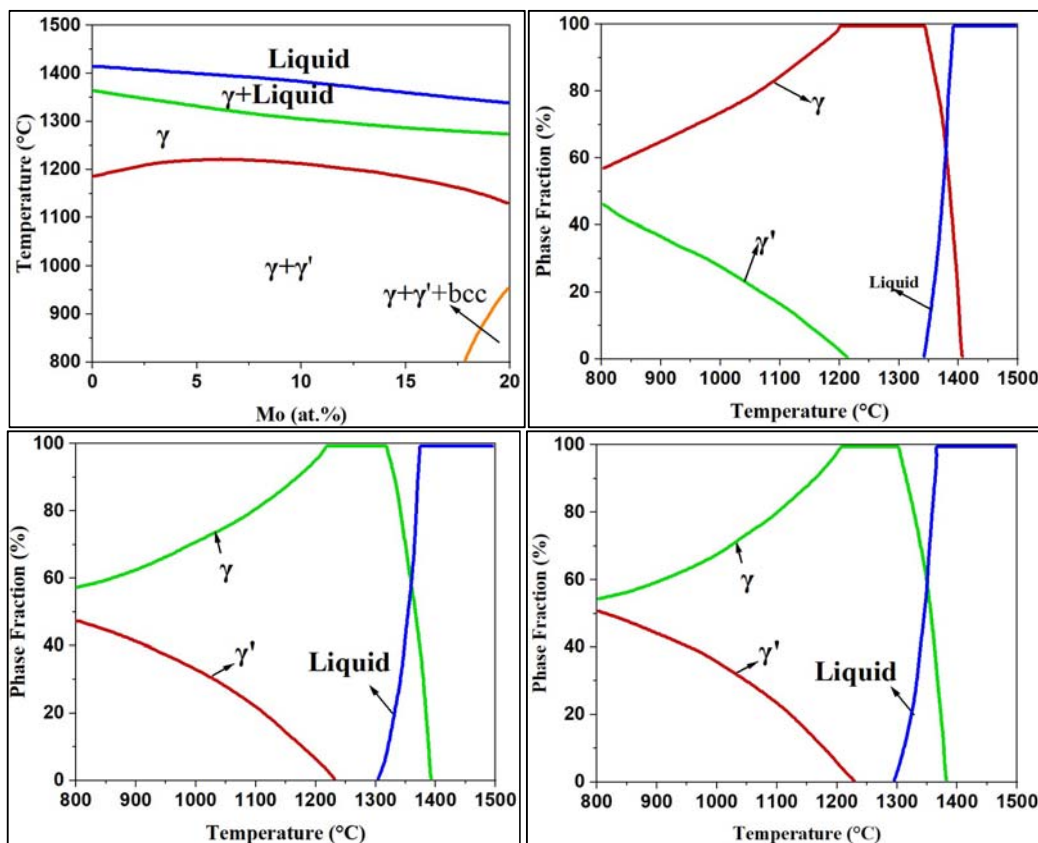

Figure 1. (a) Diagrams showing pseudo-binary phases of Fe -30 Cu -10 Si -6 W -x Mo alloy, (b)-(d) phase fractions of Fe -30 Cu -10 Si -6 W -x Mo (x: 0, 5, 10) alloys.
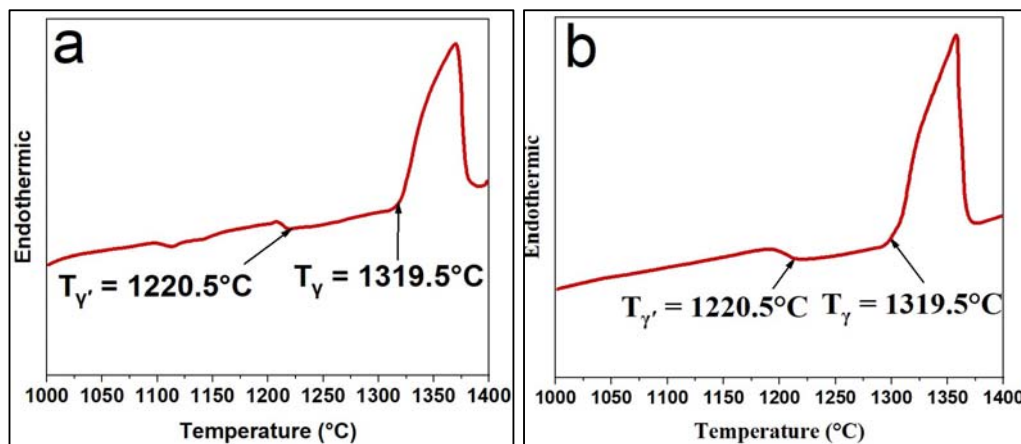
Figure 2. (a) Differential scanning calorimetry curves of Fe -30 Cu -10 Si -6 W -5Cr and (b) Fe -30 Cu -10 Si -6 W -10Cr alloy.

Fig. 2 (a, b) displays the differential scanning calorimetry curves of the 6 W 5 Mo and 6 W 10 Mo alloys. The γ' solvus temperature for 6W5 Mo alloy is 1220.5°C, while for the 6W10Mo alloy it is 1213.1°C. Each alloy has a melting point of 1319.5°C and 1300.2°C. The experimental measurements support the phase transition sites found in the phase diagram calculations and also show that the γ' solvus temperature drops marginally as the Mo content increases. This finding agrees with what found in their study of Fe - Cu - Si - W based alloys.
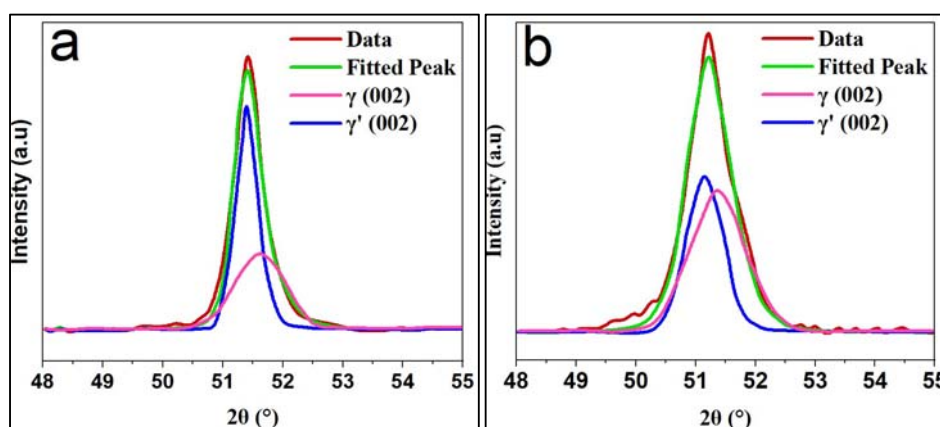

Figure 3. XRD pattern of (a) 6 W 5 Mo (b) 6 W 10 Mo alloy.

The lattice misfit, which is influenced by the γ' and γ lattice characteristics, impacts the rafting and solidity of a phase at maximum temperatures. The formula for calculating the lattice eccentric δ among the γ'/γ phases is $\delta = 2(a\gamma' - a\gamma)/(a\gamma' + a\gamma)$, where $a\gamma$ and $a\gamma'$ are the lattice factors of the γ and γ' phases [18, 19]. The 6W5Co alloy had a lattice parameter of 0.36190 nm and a 6W10Mo alloy had a lattice value of 0.36027 nm. Fig. 3(a, b) shows that the lattice misfit drops from 0.46% to 0.36% when the Mo concentration goes up from 5% to 10%. In the γ phase, lattice expansion causes the elevated value of $a\gamma$, which is mainly caused by the high partitioning impact of Mo into the γ-matrix. In most cases, the values of $a\gamma'$ are higher than $a\gamma$ in Fe-based superalloys. Lattice growth in the γ phase is directly influenced by the incorporation of γ-forming essentials, like Rhenium, Mo, and Molybdenum, which possess greater atom radius. As a result, the lattice misfit between the γ' and γ phases is diminished due to this lattice expansion [20, 21].

3.2 Coarsening γ′ precipitate behavior in Fe-30Cu-10Si-6W-10Mo alloy

After being aged for 24, 50, 100, and 200 hours, the average diameters of the γ' form in the alloy 6W10Mo were found to be 48.7" nm, 59.5 nm, 73.7 nm, 86.7 nm. The γ' phase fraction in the alloy 6W10Mo was 78.50% after 200 hours of aging, 84.27% after 100 hours, 79.51% after 50 hours, and 78.50% after 24 hours. After being aged at 800ºC, our results show that the 6W10Mo alloy can keep its small γ^' size and high γ^' phase fraction. The enhancement form of γ^' precipitate described by either the enlarged models developed from the Lifshitz-Slyozov-Wagner (LSW) theory or the traditional LSW coarsening model [22, 23]. Furthermore, a new diffusion-controlled growth model involving the γ^'/γ interface is introduced in the newly suggested TIDC coarsening theory [24]. The eq: $[s(r)]^n - [s(r_0)]^n = K(r - r_0)$ can be utilized to characterize the coarsening structure of γ^' precipitate. The γ^' precipitate at time t as the product of equivalent radius and the beginning of coarsening, denoted as r(r0) and s(r) respectively, is equal to K(r-r0), where k is the coarsening rate constant and n is the temporal exponent. Researchers can learn more about the coarsening method from the value of the temporal exponent. In contrast to the LSW model, which predicts a value of 3, the TIDC model predicts a value of 2. Logarithmic of the mean precipitation radius (log r) versus logarithmic of the aging time (log⁰t) in seconds is one technique to calculate the reverse of the temporal coefficients (1/n). The observed value of 1/n, 0.30±0.01, is near the 0.33 predicted by Lifshitz-Slyozov-Wagner model, as illustrated in Fig. 4(a). The Lifshitz-Slyozov-Wagner theory offers a reasonable clarification for coarsening behavior observed in 6W10Mo alloy. Fig. 4(b) displays a linear fitting curve that illustrates the γ^' phase's coarsening rate in 6W10Mo alloy at 800°C. The γ^' phase^' s coarsening rate at 810°C is K=0.23×10⁻²⁷ m³s⁻¹, as shown by the fitting curve's slope. Compared to the Cu-19.3Si alloy, the 10Mo alloy exhibits a lower coarsening rate of γ^' phase (K=1.4×10⁻²⁷ m³s⁻¹) which may be explained by slow diffusion of Mo in the γ matrix. The decrease dispersion rate in the 10Mo alloy is mainly caused by the strain energy of γ′/γ interface and lattice misfit of the γ′/γ two-phase in the alloy, both of which can be decreased by the presence of Mo element. Despite this, there is still a clear opportunity for enhancement when contrasted with the Fe10Si-10 tungsten alloy (K=0.09×10⁻²⁷ m³s⁻¹)
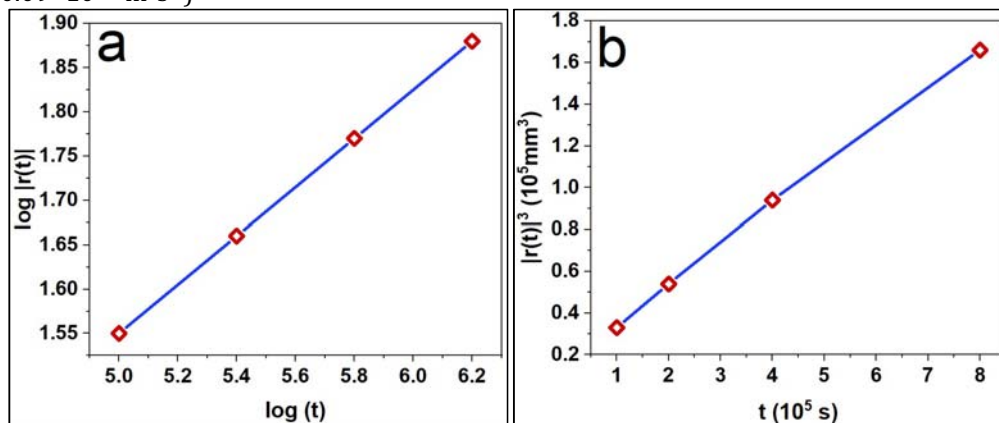
Figure 4. (a) The temporary exponents of mean size of precipitation evolution are shown by plots of log [s(r)] versus. log (r). (b) The slope values of the plots between [s(r)]3 and duration with fit data through linear regression correspond to coarsening rate constants K.

3.3 Density and CYS of Fe -30 Cu -10 Si -6 W -10Mo alloy
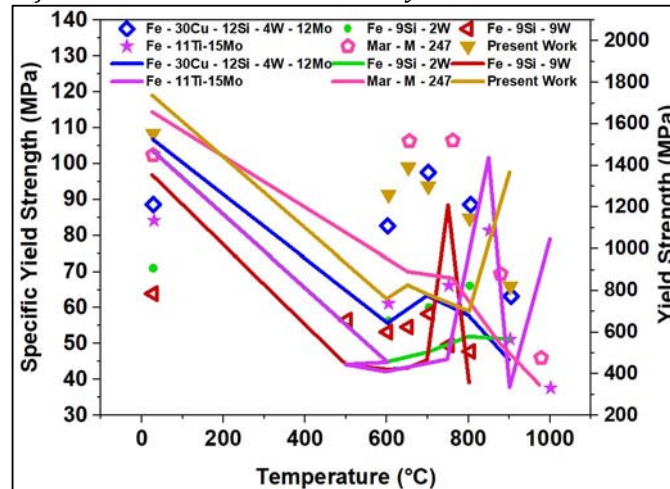
Figure 5. (a) CYS (b) specific yield strength Fe -30 Cu -10 Si -4 W -10 Mo alloy, Fe -30 Cu -12 Si -4 W -12 Mo, Fe -9Si-9 W, Fe -9Si-9 W- 2W, Fe -11W-15Mo, Mar-M– 247.

The CYS at different temperatures of the 6 W 10 Mo alloy and other superalloys based on Fe are displayed in Fig. 5. At both intermediate temperatures, and ambient temperature the 6W10Mo alloy shows a higher CYS than other Fe-based superalloys and our group's earlier Fe -30 Cu -12 Si -4 W -12Mo alloy. The yield strength of the alloy is 903 MPa at ambient temperature, which lessens to 756 MPa at 650 °C, and keeps going down as the temperature increases. The CYS of the 6 W 10 Mo alloy increases to 823 MPa at 650°C, which is an oddity. Afterwards, the yield strength drops dramatically to 534 MPa as the temperature continues to climb to 900°C. It is thought that dislocation locking at maximum temperatures causes this anomaly in CYS, which is seen in other superalloys including Cu - Si -, Fe -Titanium-, Fe - Si -W, and Fe - Si -V based alloys as well. According to the Kear-Wilsdorf mechanism, this occurrence can be described [25, 26]. In addition, high-temperature alloys provide benefits in mechanical performance and lightweight design, which are partially reflected in specific strength, a major mechanical behaviours indicator. In comparison to the other alloys mentioned before, Fig. 6 shows that at particular temperatures between room temperature and 900ºC, the 6 W/10 Mo alloy maintains some of its specific strength benefits. From a chemical standpoint, this indicates that 6 W 10 Mo alloy is the best at striking a compromise between lightweight design and mechanical performance. The coarsening rate, alloy density, and lattice misfit can be decreased with a larger Mo element percentage; nevertheless, mechanical performance may be compromised. Alternatively, alloys with a lower Mo concentration are not dense enough to be successfully reduced, which makes it difficult to meet the high-strength and lightweight design goals. In alloy composition design, finding the optimal Mo concentration is crucial for achieving a balance among mechanical performance and density. The density and γ′ solvus likewise exhibits a balanced relationship. Elements with high densities, such W, Niobium, Titanium, Molybdenum, and Rhenium, are frequently included to alloy design in an effort to improve the γ′ solvus. Nevertheless, achieving desirable mechanical characteristics and oxidation resistance while keeping the density low and boosting γ′ solvus is of utmost importance. Adding the right quantity of Mo to the Fe -30 Cu -10 Si -6 W base alloy did not considerably lower the γ′ phase melting point in this study. The inclusion of a certain quantity of Mo simultaneously reduces the density rise due to the high W content, making the alloy moderately dense. There was a complete improvement in the alloy's performance as a result of striking a balance between low density, high γ′ solvus, and mechanical behaviour.

*3.4 Oxidation resistance of Fe - Cu - Si - W - Mo alloy*
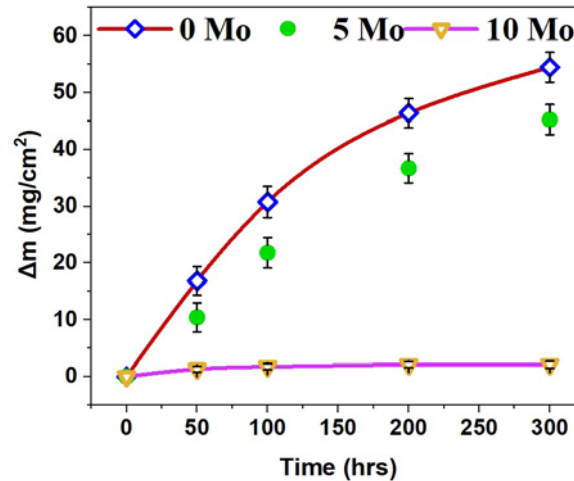
Figure. 6. Change of Mass Fe-30Cu-10Si-6W-xMo at 1000°C for (x: 0, 5, 10).

Incorporating Mo is essential for superalloys to have better oxidation resistance. The effect of Mo on the oxidation resistance of an alloy based on Fe, Cu, Si, and W was extensively examined in this work. The Fe -30 Cu -10 Si -6 W alloy undergoes a notable mass rise after extended oxidation temperature of 1000°C, as demonstrated in Fig. 6. The oxidation resistance is significantly enhanced when 5 at. % Mo is added to the alloy. However, after accounting for this enhancement, the mass change during prolonged oxidation time is still rather large. But oxidation resistance is significantly improved when Mo concentration in the alloy is raised to 10% at.%. There is little change in the alloy's bulk even after prolonged high-temperature oxidation. The 6W10Mo alloy's mass change during oxidation at 1000°C for 50 hours is just 1.32 mg/cm^2. The change of mass reaches 1.74 mg/cm^2 after 100 hours and then levels out at 2.09 mg/cm^2. The results show that the inclusion of Mo increased the oxidation resistance. It is clear that the 6W10Mo alloy has a far smaller mass change compared to commercial Cu -based superalloys like Udimet720, U720Li, Fe -9 Si -9 W-2Si-0.12B, Fe -30 Cu -9Al-6 W-4Ti-1 W -9 Mo, and Fe -30 Cu -10Si-5 W-2Si. On top of that, the 6W10Mo alloy's mass change is similar to that of Fe -30 Cu -9 Si -6 W-4Ti-1W-9Mo and Fe -30 Cu -8 Si -2 W-4Ti-1W-14Mo. Around the Fe -30 Cu -10 Si -6W and 6W5Mo alloy specimens, noticeable spalling lamellar oxide layers can be seen. The 6W10Mo alloy sample, on the other hand, shows very little spalled oxide particles. This finding lends credence to the idea that Fe - Cu - Si - W -based alloys with a greater Mo content either have a stronger binding force between alloy and oxide layer or help generate a more constant oxide layer. This indicates that the alloy's remarkable resistance to oxidation is due to its inability to create a continuous oxide layer when Mo is absent. In contrast, the 6W5Mo alloy displays Fe_2O_3, SiO_2, and WO_2 discontinuous layers. Significantly greater oxygen levels are found in areas where the concentrations of Si and Mo are higher. The resistance to oxidation 1000°C is heavily influenced by the SiO_2 and Fe_2O_3 layers, as this suggests. In addition, our results show that Mo helps Fe - Cu - Si - W -based alloys generate an effective oxide layer. As Mo is added to the 6W10Mo alloy, the outermost layer becomes predominantly Fe_2O_3, which is rich in oxygen as well. Hence, Fe_2O_3 is really important for oxidation resistance. A continuous WO_2 layer and discontinuous SiO_2 particles are present beneath the Fe_2O_3 layer. Notably, the inclusion of Mo improves the oxide layer's strength and adherence, leading to a significant decrease in cracks. Mo increases the binding strength of oxide and alloy layers, stimulates the production of SiO_2, WO_2, and Fe_2O_3 layers, prevents fracture creation, and greatly increased the oxidation resistance of Fe-Cu-Si-W alloys, according to these results taken collectively.

To further understand the 6 W 10 Mo alloy's oxidation behaviour at 1000°C for diverse time intervals, this study takes into account its persistent oxide layer and exceptional resistance to oxidation. When comparing the distribution of Si, W, and Mo elements during the 50-hour oxidation phase to the original 100-h oxidation time duration at 1000°C, the elemental dispersion study reveals no substantial difference. On the other hand, the outermost oxide layer does include a trace amount of Mo and Cu. At the oxidation procedure at 1000°C for up to 100 hours, the elements Cu and Fe start to disperse into the initially continuous Fe_2O_3 layer. Significant alterations in the oxide layers' shape and elemental mapping take place following 200 hours of oxidation at 1000°C. Because the concentration of topmost Mo drops so dramatically, the once continuous Mo-rich layer becomes discontinuous. Two separate layers rich in Si formed as a result of the substantial outward diffusion of Si at this oxidation stage is thought to be responsible for these phenomena. A continuous Al-rich layer is formed when the fast-ascending section of Si achieves the topmost layer, breaking the continuity of Mo -rich layer. So, it's safe to assume that the top oxide layer has a lot of Cr and Al and a few trace amounts of Fe and Cu. The oxygen distribution, a key component of oxidation, confirms that the top oxide layer is made of tightly packed SiO_2 particles. Additionally, a clearly expanded WO_2 layer encases the ascending SiO_2 particles, suggesting that Ta elements gradually diffuse outward during oxidation. After 300 hours of oxidation, the alloy shows a layering phenomenon similar to the Si -rich layer, which is caused by the increased tendency of W to spread outward. The ensuing upward diffusion of W interrupts the Si -rich layer in the outermost region, just as it did in the prior Mo -rich layer. The Mo -rich layer grows and a separate Mo -deficient layer forms between it and matrix as the oxidation time increases, which is an important observation. This suggests that during this oxidation stage, the Mo element also shows evidence of upward diffusion. From these findings, we have deduced that different elements undergo oxidation by a sequential diffusion and stacking process. Additional research into phases in various oxidation layers is being out in order to understand the process that supports the 6W10Mo alloy's strong oxidation resistance.
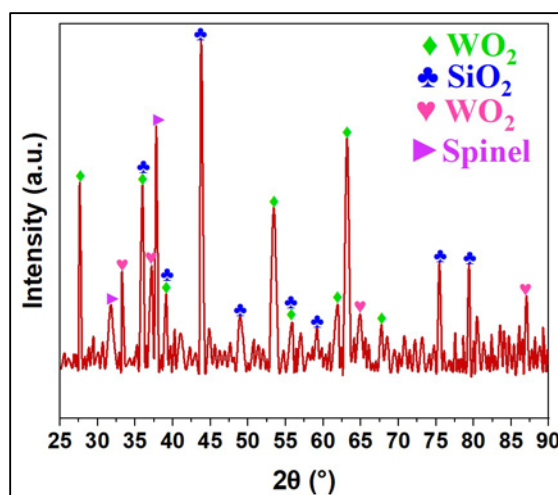
Figure 7. The X-ray diffraction pattern of Fe -30 Cu -10 Si -6 W -10 Mo alloy particles at 1000°C after oxidation for 100 hours.

After 100 hours of oxidation at 1000°C, the XRD pattern of the alloy powders is shown in Fig. 7. The alloy now contains SiO_2, Fe_2O_3, WO_2, and a spinel phase as a consequence of the oxidation process. Research has shown that these oxides are essential for making the alloy more resistant to oxidation at high temperatures [27, 28]. Table 1 shows the chemical compositions of the points that were chosen in Fig. 8.

Table 1. Chemical composition at the points indicated in Fig. 8 was determined using EDX points analysis.

| Oxidation time | Region | Element content (at. %) | | | | | | Phases |
		Fe	Cu	Si	W	Mo	O	
50 h	1	10.12	2.35	6.68		34.4	61.91	Fe_2O_3
	2	3	0.57	3.62	52.61	3.64	53.01	WO_2
	3	9.7	6.25	37.01	1.93	1.27	60.38	SiO_2
100 h	4	12.82	5.75	18.66	2.65	19.52	61.37	Spinel
	5		0.82	5.52	50.1	4.3	53.91	WO_2
	6	2.84		39.04		4.42	67.76	SiO_2
	7	9.08	7.08	21.73	1	7.53	71.51	Spinel
	8	0.69	0.54	39.83	0.95	0.89	68.67	SiO_2
	9			8.89	38.38	6.02	60.78	WO_2
200 h	10	49.84	33.3			7.79	12.77	Matrix
	11	1.04		43.07			65.96	SiO_2
	12	29.53	27.89		51.57	0.9	9.06	Oxides enriched with W, Fe, Cu
	13	14.82	9.07	28.21	4.29	7.93	54.79	Spinel
	14	2.03	0	5.88	18.77	18.75	69.21	Oxides enriched with W, Mo, O
	15	0	0.59	31.9	9.08	5.29	68.39	SiO_2
	16	6.18		25.81		9.16	67.39	SiO_2
300 h	17				30.63	11.57	69.23	Oxides enriched with W, Mo, O
	18	3.31	2.36	0	26.47	17.01	65.64	SiO_2
	19	7.65	2.48	3.4	35.27	9.29	56.08	WO_2
	20	50.93	33.05	3.85	14.36	6.64	14.22	Matrix
	21	1.26	0.74	40.51		0.47	68.01	SiO_2
	22	30.3	25.88		55.21	0.75	6.06	Oxides enriched with W, Fe, Cu

At 1000°C during the initial stage of oxidation (0-50 hours), the outmost layer had a continuous Fe_2O_3 layer, while discontinuous SiO_2 particles and W oxide were situated beneath it. After oxidation for 100 hours, the alloy's Fe, W, and Si diffusion becomes more noticeable, causing the outmost oxide layer to gradually change from continuous Fe_2O_3 to a (Fe, Cu) (Si, Mo)2O4 spinel phase. As Ta diffuses across the WO_2 layer, its width increases significantly. The SiO_2 particles then climb with an inclination to pierce the WO_2 layer. The SiO_2 layer begins to show signs of stratification after 200 hours of oxidation. Below the spinel layer, there is a continuous SiO_2 layer where some of the quickly diffusing Si components are trapped, and there is also a larger Ta-rich layer [29]. The stratification of the W-rich layer is likewise quite limited at this oxidation stage, which is intriguing. Although some of the W oxide increases below the continuous SiO_2 layer, it has been confirmed that the W -rich layer, which contains SiO_2 particles, is rich in W, Fe, and Cu. The fast diffusion of W sets off a chain reaction at the 300-hour oxidation milestone. The W, Mo, and Cu-enriched continuous oxide layer starts to fracture. Even more, the WO_2 particles expand outward. Underneath the spinel and discontinuous SiO_2 layers, EDS examination also shows a continuous oxide layer that is enhanced with W, Mo, and O.

This finding provides more evidence that the formation of a spinel layer on the surface of the alloy during prolonged oxidation slows the growing rate of oxides [30]. On the surface of the alloy, a continuous spinel layer sequence, SiO_2 layer, oxides enhanced with W, Mo, and the sequential stratification of Si and W at diffusion results in the formation of oxygen scale. Therefore, it is reasonable to assume that the oxide growth curve gradually flattens when there are several continuous oxide layers since their presence further reduces the rate of oxide growth [31, 32]. At the beginning of the oxidation process, the substrate is in touch with the lowest SiO_2 particles, and there are also some scattered SiO_2 particles inside the substrate. Previous related reports have also made similar observations [30]. The presence of SiO_2 and Fe_2O_3 as significant oxidation products in the Fe - Cu - Si - W based superalloy is suggested by the fact that the Oxygen elements are mostly concentrated in Si / Mo rich scale. A significant influence on oxidation resistance may result from their distribution in the oxide layer [33, 34].
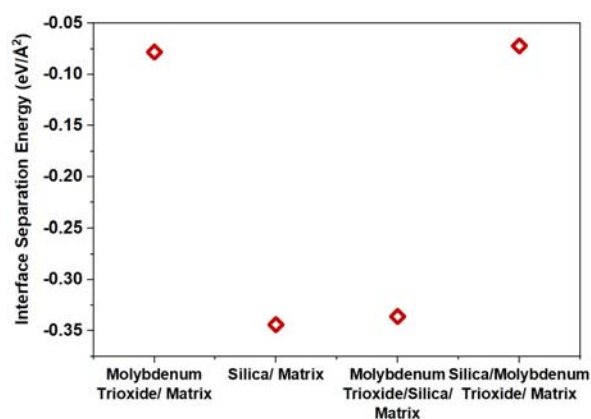
Figure 8. Interface separation energies.

In order to learn where the energy for the initial distribution of SiO_2 and Fe_2O_3 oxide layers in the 6W10Mo alloy came from, we ran AIMD simulations. The energy required to separate the four oxide layer configurations that come into contact with the matrix are shown in Fig. 8. The results are unaffected by the simplification of the matrix here into an FCC-CuFe solid solution. It is noticeable that the interface particular energy of SiO_2 with the matrix – 0.37 eV/Å2, which is much greater than Fe_2O_3's (-0.09 eV/Å2) when it comes into contact with the matrix. What this means is that SiO_2 has a greater propensity to form bonds with the matrix than Fe_2O_3 [35, 36]. Additionally, when SiO_2 is in touch with the matrix, the binding strength between the two materials is unaffected by the Fe_2O_3 layer, which guarantees that the oxide layer covered matrix will remain stable. These numerical findings lend theoretical credence to the oxide layer's structure during the alloy's first oxidation stage, clarifying why Si is found at the oxide layer's base and scattered over the matrix interface. Due to their lower potentials, Si and W combine with O to form oxides as the oxidation period advances, and Oxygen atoms continue to migrate inward [37]. Oxides containing Si and W (SiO_2, WO_2) rise significantly and undergo stratification.

4. Conclusions

Thermodynamic phase simulations were used to generate a Fe -30 Cu -10 Si -6 W -10 Mo alloy, which was subsequently named 6W10Mo, and it had remarkable all-around qualities. The impacts of Mo on microstructure, γ′ solvus, lattice misfit, as well as oxidation resistance were much studied and debated.

From this, we can infer that:

- According to the results of the thermodynamic calculations, the γ' solvus rises at the beginning and then steadily falls as Mo is added. After the Mo content is around 10%, the alloy shows γ' solvus that is relatively stable, and the γ' phase fraction doesn't drop much. There was a high degree of concordance between the predicted and observed outcomes. Mo also decreased the coarsening rate and improved the microstructure. A strong γ-phase producing element, Mo was found to aid in reducing the lattice eccentric among γ and γ' form, which in turn improves the microstructure stability.
- The appropriate amount of Mo was added to the alloy to balance its density, melting temperature, and mechanical behaviours of γ' phase in the superalloy. A maximum γ' solvus (1208°C), comparatively minimum density (8.78 g/cm^3), and moderate CYS (821 MPa at 650°C) are all outcomes of this, which contribute to its outstanding overall performance.
- Adding Cr to Fe - Cu - Si - W -based alloys considerably lowers the weight gain caused by oxidation 1000°C and considerably enhances their resistance to oxidation. The inclusion of Cr primarily promotes the creation of a continuous Fe_2O_3 layer and SiO_2, which is responsible for this enhancement. Adding Cr also makes the oxide layer more resistant to spalling by reducing the frequency of cracks and improving the bond between oxide layer and alloy.
- Upon reaching 1000°C, the 6W10Mo alloy demonstrates remarkable resistance to oxidation. The elements Si and W move towards the top layer after extended oxidation at 1000°C. SiO_2 and WO_2, which were initially mixed, eventually separate into their own layers. A W, Mo, and Oxygen-enhanced oxide scale, an SiO_2 layer, and a continuous spinel layer are eventually generated. Some have hypothesized that this alloy's remarkable oxidation resistance is due to the existence of many oxide layers.

References

[1]   Zhu Z *et al* 2023 *Adv Eng Mater* **25**
[2]   Li Y M *et al* 2022 *Metals and Materials International* **28** 2305
[3]   Wang C *et al* 2024 *Mater Des* **238**
[4]   Ponnusamy Prasanth *et al* 2023 *Journal of Physics: Conference Series* **2603** 012039
[5]   Sathiaraj G *et al* 2016 *ARPN Journal of Engineering and Applied Sciences* **11** 6056
[6]   Liu Y *et al* 2020 *Acta Mater* **195** 454
[7]   Yen S Y *et al* 2023 *J Alloys Compd* **952**
[8]   Babu B *et al* 2023 *Journal of Physics: Conference Series* **2603** 012041
[9]   Wang K *et al* 2023 *J Alloys Compd* **952**
[10]   Mahmoud H M A *et al* 2022 *Advances in Materials Science and Engineering* **2022**
[11]   Dinesh Kumar D *et al* 2023 *J Chem* **2023**
[12]   Srinivasan R *et al* 2023 *Advances in Materials Science and Engineering* **2023**
[13]   Jery A E *et al* 2023 *Water* **15**
[14]   Girimurugan R *et al* 2022 *Journal of Ceramic Processing Research* **23** 553
[15]   Seenivasan S *et al* 2024 *AIP Adv* **14**
[16]   Song Z *et al* 2022 *Chinese Journal of Lasers* **49**
[17]   Srividya K *et al* 2024 *International Journal on Interactive Design and Manufacturing* **18** 1459
[18]   Ma K *et al* 2023 *Acta Mater* **257**
[19]   Jayaraman R *et al* 2023 *AIP Conference Proceedings* **2521**
[20]   Prasanth I S N V R *et al* 2023 *J Nanomater* **2023**
[21]   Manikandan R *et al* 2023 *Mater Today Proc*
[22]   Cui P *et al* 2023 *Materials* **16**
[23]   Yen S Y *et al* 2020 *Calphad* **70**
[24]   Zhuo H *et al* 2024 *J Alloys Compd* **1001**
[25]   Vinoth S *et al* 2023 *Journal of Physics: Conference Series* **2484** 012012
[26]   Gao L *et al* 2024 *Adv Eng Mater* 2400687
[27]   Sridar S *et al* 2023 *Minerals, Metals and Materials Series* 755
[28]   Wang C *et al* 2024 *Mater Des* **238**
[29]   Vairavel M *et al* 2020 *AIP Conference Proceedings* **2283**

[30] Rathinam R *et al* 2022 *J Nanomater* **2022**
[31] Shafiee A *et al* 2020 *Metals and Materials International* **26** 591
[32] Qiu C *et al* 2021 *Calphad* **74**
[33] Degnah A *et al* 2024 *Mater Res Express* **11**
[34] Xu B *et al* 2022 *Mater Today Commun* **30**
[35] Krishnan V K *et al* 2023 *Materials Today: Proceedings*
[36] Ma K *et al* 2023 *Acta Mater* **257**
[37] Wu W *et al* 2022 Acta Mater **233**